A novel phase-field based formulation of interface evolution during mechanical compaction of sedimentary basins

Kunal Bhagat [1], Zirou Jin [2] Shiva Rudraraju [3,*]

Abstract

A novel phase-field method based numerical approach to modeling the compaction process of sediments is presented. Water-logged rock or soil sediments are deposited on the water basins over time and the increasing volume of the sediment compacts under its own weight and external pressure. Coupled evolution of mass conservation, Darcy flow, and the viscoelastic constitutive response, in conjunction with the evolution of porosity and permeability, make this problem highly non-linear and involve moving boundaries. We adopt a phase-field approach to represent the moving sediment interface, and the underlying multiphasic model permits for studying compaction in dynamically evolving sediments. This approach does not necessitate a change of domain sizes as is the case of existing traditional models of sedimentation but rather treats sedimentation growth as a problem of interface motion. We first model a classical compaction problem in 1D to compare with existing results in the literature, and then extend the framework to 2D to model the compaction process taking place under the influence of gravity. The model is then extensively applied to understand the effect of the sediment initial state and the sediment material properties on the compaction process and its spatiotemporal evolution. Lastly, a strong validation of our phase-field treatment results against predictions from traditional methods of solving open boundary sediment compaction problems, and a good agreement between the conventional understanding and the numerical predictions of porosity dependence on the fluid pore pressure for various cases of geological interest, are used to demonstrate the applicability and scalability of this novel numerical framework to model more advanced sediment compaction problems and geometries.

Keywords: finite element method, poroelasticity, moving interface, order parameter

[1] Graduate Student, Department of Mechanical Engineering, University of Wisconsin-Madison
[2] Graduate Student, Geological Engineering and Department of Civil and Environment Engineering, University of Wisconsin-Madison
[3,*] Department of Mechanical Engineering, University of Wisconsin-Madison; corresponding author

 doi:10.20944/preprints202212.0093.v1

1 Introduction

The consolidation of sediments like rock, sand, clay, or shales is an important natural process that takes place at a geological time scale [1]. Sediments slowly deposit through erosion and transport processes aided by wind, flowing water and ice. The consolidation and compaction of these materials are caused by the increasing pressure exerted by the weight of the overlying deposits. Further, mechanical compaction results in partial expulsion of fluid from the pores in these sedimentary materials. As a result, high pore pressure is experienced by the trapped fluid in the pores if the fluid is constrained from draining out. The knowledge of the sediment compaction and abnormal pore pressure existing in rocks is significant for success of drilling in the oil exploration industry [2]. Damaged rocks around major fault zones also undergo cycles of damage creation and healing/compaction [3], where the associated pore pressure changes can have significant consequences on the stability of the seismogenic faults. In a grander context, understanding sediment compaction is also relevant to climate change studies as any major subsidence in coastal areas can potentially compound the risks associated with rising sea levels [4].

An academic inquiry into the behavior of soils and the sediments under loading can be traced back to the work on soil subsidence under the effect of positive effective stress by Terzaghi [5]. Poroelasticity model for rocks and modification to the concept of effective pressure was introduced in the work of Biot [6]. The work of Gibson [7] on the clay consolidation was instrumental in this field. The author dealt with the one-dimensional consolidation of the clay layer using linear integral equations. Further investigation into the process of creation of abnormally high pore pressure in the sediments was done by Bredehoeft *et al.* [8] using linear integral equation solutions. A breakthrough numerical model studying the shale compaction and high pore fluid pressure was formulated by Smith [9]. Their model accounted for permeability-porosity dependence, Darcy law, and variable pore fluid viscosity.

The growing consensus in the community was that abnormally high pore fluid pressure was a result of not only the mechanical compaction, but several physical and chemical processes were also at play. An asymptotic and numerical analysis of compaction in the sedimentary basin was carried out by Audet *et al.* [10]. In their work, they formulated a generalized model, building on the work of previous authors by outlining rheological, thermal, and diagenetic aspects of the sediment compaction process. The limits of the non-linear behavior of porosity and effective pressure at greater depth and consideration of pressure solution were highlighted in the work of Fowler *et al.* [11]. Mechanical and mechano-chemical compaction of the sedimentary basin was studied by Schneider *et al.* [12] to show porosity dependence on time and temperature. They numerically solved the model considering the elastoplastic model, temperature-dependent sediment viscosity, and porosity effective stress rheology relationships. On a similar ground, the analytical work by Yang [13] is relevant. A Maxwell type viscoelastic constitutive model of the sediment, coupled with a non-linear relation between the effective pressure and porosity were the key features adopted in

 doi:10.20944/preprints202212.0093.v1

the subsequent numerical works.

The focus of most literature in this field is on formulating more rigorous constitutive models. The complexity of these models then limits the possibility of closed-form solutions and hence numerical methods are desired. This was studied rigorously in the work of Bethke *et al.* [14] and it was shown that analytical solution exist for the linear problem and a numerical solution is sought when the governing equations are non-linear when representing more realistic geological conditions. The characteristic sediment compaction process is an open boundary problem due to the involvement of sediment deposition. The finite difference method and the finite element method are the most common numerical techniques used to solve the governing equations of the compaction problem. The consolidation of soil using the theory presented by Biot [6] is studied using a finite layer method by Mei *et al.* [15]. Their model can be successfully applied to estimate immediate and final soil settlement as well as consolidation settlement of cross-anisotropic soil. Nogami *et al.* [16] developed a meshfree numerical method for studying consolidation of lumpy clay. A finite difference method based numerical model by Keith et al. [17] is an important model that was used to study overpressuring in shales, along with a moving boundary representation. Suetnova and Vasseur *et al.* [18] uses the finite difference method to solve the open boundary problem, but the treatment of the growing sediment height follows conventional methods of changing the computational domain. Morency *et al.* [19] developed a 2D numerical model for studying compaction using viscoplastic deformation in the context of disequilibrium compaction and delta stability. They use the finite element method and present a comparison of their results with published results on 1D compaction. Their treatment of the moving boundary was the same as in Suetnova and Vasseur[18]. Mechanical compaction is considered using a finite poro-plasticity model and solved using the finite element method by Bernaud *et al.* [20]. They developed a numerical model where activation-deactivation of a region is enforced, thereby turning an open system into a closed one. In the work of Maghous *et al.* [21], a relatively better version of activation-deactivation is applied to model sedimentary basin growth by modifying the solid and fluid density within the mesh elements. Wangen *et al.* [22] made use of toggle switch cellular automation method to model fluid expulsion along with local micro-fracturing and redistribution of pore fluid. In this context, the numerical model we propose in this work is more sophisticated and accurate, as we get rid of explicit bookkeeping of the boundary location and no explicit activation/deactivation of any region or modifications of material properties in the mesh elements is needed. Further, our model does not require an initial small sediment height to begin computations as opposed to many of the conventional methods described above.

In this work, we present a novel numerical approach to solve the compaction process active in sediments. We adopt a phase-field approach to represent the moving sediment interface, and the underlying multiphasic model permits for studying compaction in dynamically evolving sediments. This approach does not necessitate a change of domain sizes as is the case of existing traditional models of sedimentation but rather treats sedimentation growth as a problem of interface motion.

 doi:10.20944/preprints202212.0093.v1

We first model a classical compaction problem in 1D to compare with existing results in the literature, and then extend the framework to 2D to model the compaction process taking place under the influence of gravity. The model is then extensively applied to understand the effect of the sediment initial state and the sediment material properties on the compaction process and its spatiotemporal evolution.

The manuscript is organized as follows: In Section 2 we present the mathematical basis of sediment compaction, followed by a presentation of the governing equations under the classical formulation of sedimentary compaction in Section 3. We then propose a novel phase-field based numerical treatment of the sedimentary compaction process in Section 4. This is followed by the validation studies and extensive applications of the phase-field model to understand the effect of the sediment initial state and the sediment material properties on the compaction process in Section 5. Finally the concluding remarks are presented in Section 6.

2 Mathematical basis of sediment compaction

In this section, we first briefly describe the physical process of sediment compaction. We then present the classical governing equations for a purely mechanical compaction process in sediments. As one can observe, these classical treatments involve explicit movement of the sediment interface by changing the computational domain with time. To remove this significant drawback of evolving the computational domain, we adopt a diffuse interface treatment of the interface, and present a novel phase-field formulation of the sediment compaction problem and its numerical framework.

2.1 Problem description

The sediment compaction process, in general, is thermodynamically an open system due to the (1) rising height of the sediment, (2) subsidence of the compacted sediment base, and 3) exchange of mass across the boundaries. In the given control volume, we treat a sediment column as a porous matrix structure. The solid part of the matrix is assumed to be made of dry sediment material, and the pores are assumed to be filled with any type of fluid with dissolved mineral and salts, not necessarily pure water. The sediment column height can rise due to the deposition of the waterlogged sediments on the existing porous structure. The base of this slowly growing column can sink due to the subsidence prevalent in the underlying geological structure. The solid and fluid matter occupying the porous region are subjected to compressive loading exerted by the weight of the overlying material. This porous system of sediments then undergoes significant volumetric compaction, consolidation, and cementation, which are considered to be significant changes to the underlying material structure of the sediment. In this section, we limit our inquiry to purely mechanical deformation. Although the solid and fluid matter within the pores is treated as incompressible, the pores themselves can undergo considerable shrinking and hence their can be

Preprints (www.preprints.org) | NOT PEER-REVIEWED | Posted: 6 December 2022 doi:10.20944/preprints202212.0093.v1

a reduction in the volume of the sediment. In modeling this problem, these changes need to be understood in the presence of spatial and temporal variations of porosity, pore fluid pressure, and the velocity of the fluid.

2.2 Governing equations for the mechanical compaction process

In this section, we present a model considering the purely mechanical compaction process of sediments. Temperature dependence and the chemical changes are neglected in this work. The model accounts for the three physical processes of (1) mass conversation of the solid and the fluid, (2) Darcy's law for fluid flow and its dependence on the permeability and pressure drop in the porous region, and (3) a viscoelastic Maxwell rheology law as the constitutive model for the underlying deformation.

In the mathematical expressions presented in this manuscript, bold faced symbols and operators denote vector or tensorial quantities and operators, respectively.

2.2.1 Mass conservation

Assuming the sediment material to be a porous system, the pores are occupied by a fluid. The solid region can consist of clay, rocks, shales, etc. Assuming no loss of either the fluid or the solid mass, conservation of mass is described by the Equations 1-2. Here ϕ denotes the porosity, ρ_f and ρ_s are the fluid and the solid density, respectively, and $\boldsymbol{V}_f$ and $\boldsymbol{V}_s$ are the fluid and the solid velocity, respectively, and t denotes time,

$$\frac{\partial \phi \rho_f}{\partial t} + \boldsymbol{\nabla} \cdot (\phi \rho_f \boldsymbol{V}_f) = 0 \tag{1}$$

$$\frac{\partial (1-\phi) \rho_s}{\partial t} + \boldsymbol{\nabla} \cdot \big((1-\phi) \rho_s \boldsymbol{V}_s\big) = 0 \tag{2}$$

2.2.2 Darcy's law

The velocity of the fluid in the porous medium is governed by the pressure differential across the medium. The solid region is not stationery, so we consider fluid velocity with respect to the solid velocity. Now, using the classical Darcy's equation, we express the fluid velocity as follows:

$$\boldsymbol{V}_f - \boldsymbol{V}_s = -\frac{k}{\phi \mu_f} \big(\boldsymbol{\nabla} P_f + \rho \mathbf{g}\big) \tag{3}$$

where,

$$\mathbf{q}_d = \phi(\boldsymbol{V}_f - \boldsymbol{V}_s) \qquad P_{ex} = (P_f - P_h) \qquad \mathbf{q}_d = -\frac{k}{\mu_f} \big(\boldsymbol{\nabla} P_{ex}\big)$$

Preprints (www.preprints.org) | NOT PEER-REVIEWED | Posted: 6 December 2022 doi:10.20944/preprints202212.0093.v1

Here, $\mathbf{q}_d$ is the seepage velocity, P_{ex}, P_h and P_f are the excess fluid pressure, hydrostatic pressure and the pore fluid pressure, respectively. $k = k_0(\frac{\phi}{\phi_0})^m$ is the permeability dependent on the porosity, and $\mathbf{g}$ is the gravitational acceleration. A detailed description of the domain specific notions of excess fluid pressure and pore fluid pressure can be found in the literature on sedimentary basins [11, 13, 23].

2.2.3 Constitutive model for mechanical deformation

Following the works of [13, 18, 19], we choose the Maxwell viscoelastic rheology as the relevant constitutive model for this compaction problem. The porous structure of the sediment undergoes deformation which is accounted for in the volumetric strain, and the total volumetric strain is a sum of the volumetric strains generated from the elastic response and the viscous response. The total pressure felt by the porous structure is balanced by the pressure in the solid matrix and the fluid pressure in the pores. Thus we have, as the total pressure, $P_t = P_e + P_f$, where P_e is the effective pressure that results in the deformation of the sediment [24]. The porosity of the system is given by $\phi = \frac{\Omega_f}{\Omega_T}$, where Ω_f and Ω_T are the pore fluid volume and the total bulk volume. Assuming the solid medium is incompressible and the volume change is reflected in the decrease of the pore volume, we have $\Omega_T = \Omega_f + \Omega_s$ and $d\Omega_T = d\Omega_f$. With this background, we now present a brief derivation of the relevant viscoelastic constitutive law.

$$d\phi = \frac{d\Omega_f}{\Omega_T} - \Omega_f \frac{d\Omega_T}{\Omega_T^2} = \frac{d\Omega_f}{\Omega_T} - \phi\frac{d\Omega_T}{\Omega_T} = (1-\phi)\frac{d\Omega_T}{\Omega_T}$$

but considering bulk compressibility, $\beta_b = -\frac{1}{\Omega_T}\left(\frac{\partial\Omega_T}{\partial P_e}\right)$, we have

$$d\phi = -(1-\phi)\beta_b \partial P_e$$

$$\Rightarrow \frac{d\phi}{dt} = -(1-\phi)\beta_b \frac{dP_e}{dt}$$

Further, the bulk compressibility and pore compressibility are related as $\beta_b = \phi\beta_p$, where pore compressibility is given by $\beta_p = -\frac{1}{\Omega_p}\left(\frac{\partial\Omega_p}{\partial P_e}\right)$. From this, we get:

$$\frac{1}{(1-\phi)}\frac{d\phi}{dt} = -\phi\beta_p\frac{dP_e}{dt}$$

Now the constitutive creep law describing the evolution of the volumetric strain rate caused by the effective pressure can be be written as follows:

$$\frac{1}{(1-\phi)}\frac{d\phi}{dt} = -\frac{P_e}{\xi}$$

where $\xi = \frac{\eta}{\phi}$ is the viscosity of the porous structure, and η is the solid viscosity. As can be seen, the volumetric strain rate is expressed here in terms of the change in porosity. Finally, combining

Preprints (www.preprints.org) | NOT PEER-REVIEWED | Posted: 6 December 2022 doi:10.20944/preprints202212.0093.v1

the mechanical compaction of pores and the viscous creep, we get the following Maxwell model formulation,

$$\frac{1}{(1-\phi)}\frac{d\phi}{dt} = -\phi\beta_p\frac{dP_e}{dt} - \phi\frac{P_e}{\eta} \tag{4}$$

Equations 1-4 are the governing equations for modeling mechanical compaction in any general domain geometry. However, as we will see in the following section, analytical solutions are only available for the one dimensional equivalent of this model. Thus, to validate our phase-field framework for modeling mechanical compaction during sedimentation using classical analytical solutions, we reduce the above governing equations into their one dimensional equivalent in Section 5.1. This reduction to a one dimensional domain is only for the purpose of validation, and later, removing these restriction, we present results for 2D geometry. It is important to note that, one dimensional models of mechanical compaction are the standard in the sedimentary compaction field, and they have traditionally been relied on for gaining important insights into the compaction process.

3 Classical formulation of sedimentary compaction

Equations 1-4 are the general governing equations for modeling the mechanical compaction process. In these equations, $\phi, \boldsymbol{V}_s, \boldsymbol{V}_f, P_e, P_f$ and P_t are the unknown variables. As stated in the problem description in Section 2.1, we have a moving boundary in this problem. The deposition of the waterlogged sediments with a known deposition velocity, $\boldsymbol{V}_0$, from the top. The base of the sediment sinks with known subsidence velocity, $\boldsymbol{V}_1$. Using the incompressibility of the solid and the fluid matter, their densities, ρ_s and ρ_f, are assumed to be constant. Adding Equations 1 and 2, and assuming that the fluid and solid matter are sinking with the same velocity at the bottom of the sediment column, i.e. $\boldsymbol{V}_s = \boldsymbol{V}_f = \boldsymbol{V}_1$ (a constant), we have

$$\frac{\partial \boldsymbol{V}_f\phi}{\partial y} + \frac{\partial \boldsymbol{V}_s(1-\phi)}{\partial y} = 0$$

$$\Rightarrow \boldsymbol{V}_f\phi + \boldsymbol{V}_s(1-\phi) = \boldsymbol{V}_1$$

$$\Rightarrow \boldsymbol{V}_f = \frac{\boldsymbol{V}_1 - \boldsymbol{V}_s(1-\phi)}{\phi}$$

As can be seen from the schematic in Figure 1, the sediment height is assumed to be along the y-axis, so the velocity gradients are considered only along this sediment height direction. Considering the typical sedimentation geometries that are numerically modeled, this widely valid assumption of sedimentation primarily along the height direction results in a pseudo-one dimensional physical interpretation of the model, although the governing equations and the numerical model are developed for a general 2D/3D geometry. Now, modifying Equation 3 by substituting for the fluid velocity $\boldsymbol{V}_f$ and eliminating the fluid pressure $P_f = P_t - P_e = -\rho_s\mathbf{g}\cdot\boldsymbol{y} - P_e$, we get

Preprints (www.preprints.org) | NOT PEER-REVIEWED | Posted: 6 December 2022 doi:10.20944/preprints202212.0093.v1

$$\boldsymbol{V}_s - \boldsymbol{V}_1 = -\frac{k}{\mu}\left(\frac{\partial P_e}{\partial \boldsymbol{y}} + (\rho_s - \rho_f)\mathbf{g}\right) = -\frac{k}{\mu}\left(\frac{\partial P_e}{\partial \boldsymbol{y}} + \Delta\rho\mathbf{g}\right)$$

In the chosen Lagrangian frame of reference, we work with the material derivative $\left(\frac{D}{Dt} = \frac{\partial}{\partial t} + \boldsymbol{V}_s \cdot \frac{\partial}{\partial \boldsymbol{y}}\right)$. This will result in the following modification to mass conservation, that was earlier represented by Equation 2,

$$\frac{\partial(1-\phi)}{\partial t} + \boldsymbol{\nabla} \cdot ((1-\phi)\boldsymbol{V}_s) = 0$$

$$\Rightarrow \frac{\partial \phi}{\partial t} + \boldsymbol{V}_s \cdot \boldsymbol{\nabla}\phi - (1-\phi)\boldsymbol{\nabla} \cdot \boldsymbol{V}_s = 0$$

$$\Rightarrow \frac{1}{(1-\phi)}\frac{D\phi}{Dt} = \boldsymbol{\nabla} \cdot \boldsymbol{V}_s \tag{5}$$

$\left(\boldsymbol{V}_s - \boldsymbol{V}_1\right)$ is replaced with the relative velocity of solid in the Lagrangian frame of reference, $\boldsymbol{V}_s^r$, denoted as just $\boldsymbol{V}_s$ for convenience

$$\boldsymbol{V}_s = -\frac{k}{\mu}\left(\frac{\partial P_e}{\partial \boldsymbol{y}} + \Delta\rho\mathbf{g}\right) \tag{6}$$

With this, the Maxwell constitutive model, given earlier by Equation 4, now modifies to:

$$\phi\beta_p\frac{DP_e}{Dt} = -\frac{\phi}{\eta}P_e - \frac{1}{(1-\phi)}\frac{D\phi}{Dt}$$

$$\phi\beta_p\frac{DP_e}{Dt} = -\frac{\phi}{\eta}P_e - \boldsymbol{\nabla} \cdot \boldsymbol{V}_s \tag{7}$$

We now pose the above governing equations in a non-dimensional form. In the context of these equations, the dimensionless form is helpful for the subsequent numerical modeling, due to the otherwise large magnitudes of the geological length and time scales involved in a dimensional form. Choosing the appropriate scaling parameters [18], Table 2 lists the relevant dimensionless parameters. Here, L, T, P, β_p and ϕ_0 are the characteristic - length, time, pressure, pore compressibility, and porosity, respectively. Using these dimensionless parameters, the non-dimensional governing equations are given by:

$$\frac{D\tilde{\phi}}{D\tilde{t}} = (\alpha - \tilde{\phi})\boldsymbol{\nabla} \cdot \tilde{\boldsymbol{V}}_s \tag{8}$$

$$\tilde{\boldsymbol{V}}_s = -\tilde{\phi}^3\left(\frac{\partial \tilde{P}_e}{\partial \tilde{\boldsymbol{y}}} + \mathbf{1}\right) \tag{9}$$

$$\tilde{\phi}\tilde{\beta}\frac{D\tilde{P}_e}{D\tilde{t}} = -\frac{\tilde{\phi}}{\tilde{\eta}}\tilde{P}_e - \tilde{\boldsymbol{\nabla}} \cdot \tilde{\mathbf{V}}_s \tag{10}$$

Preprints (www.preprints.org) | NOT PEER-REVIEWED | Posted: 6 December 2022 doi:10.20944/preprints202212.0093.v1

where $\tilde{\phi}$, $\tilde{\boldsymbol{V}}_s$ and $\tilde{P}_e$ are the dimensionless porosity, relative solid velocity, and effective pressure, respectively. For completeness, here we also specify the boundary conditions for this moving interface problem. At the top moving interface, $\tilde{P}_e = 0$, and $\tilde{\phi} = 1$. The new frame of reference is attached to the base of the sediment and hence solid velocity satisfies $\tilde{\boldsymbol{V}}_s = 0$ at the base.

Parameter	Expression	Description
L	$\sqrt{\frac{\eta_0 k_0 \phi_0^{m-d}}{\mu}}$	Characteristic length
P	$\Delta\rho g L$	Characteristic pressure
T	$\frac{\eta_0}{P\phi_b^d}$	Characteristic time
$\tilde{\beta}$	$\beta P \phi_0 = \frac{\beta\eta_0}{T}$	Characteristic pore compressibility
$\tilde{\eta}$	$\frac{\eta}{\eta_0}$	Non-dimensional solid viscosity
$\tilde{\boldsymbol{V}}_0$	$\frac{\boldsymbol{V}T}{L}$	Non-dimensional interface velocity
k	$k_0(\frac{\phi}{\phi_0})^m$	Sediment permeability
$\tilde{t}$	$\frac{t}{T}$	Non-dimensional time
$\tilde{\boldsymbol{\nabla}}$	$\frac{1}{L}\boldsymbol{\nabla}$	Non-dimensional gradient operator
$\tilde{\boldsymbol{y}}$	$\frac{\boldsymbol{y}}{L}$	Non-dimensional depth
α	$\frac{1}{\phi_0}$	Inverse of characteristic porosity
m	3.0	Power exponent in the characteristic length
d	1.0	Factor in the characteristic length

Table 1: Characteristics quantities, dimensionless parameters and constants relevant to the sediment compaction problem.

4 Phase-field formulation of sedimentary compaction

In this section, we describe a novel numerical formulation that solves the sediment compaction problem involving a moving boundary. We adopt the phase-field modeling approach that is a diffuse interface method for treating moving phase interfaces. Phase-field modeling has traditionally found immense application in the modeling of materials science problems [25, 26, 27], but is now used for numerical modeling in a wide spectrum of physical disciplines. Our phase-field representation of the sedimentary domain and its moving boundary is inspired by phase-field models in the literature that use a structural order parameter to represent moving phase boundaries in problems like evolution of dendrites during solidification and evolution of cracks during fracture [28, 29]. The central merit

Preprints (www.preprints.org) | NOT PEER-REVIEWED | Posted: 6 December 2022 doi:10.20944/preprints202212.0093.v1

of the phase-field approach lies in its ability to implicitly represent a boundary or interface using an order parameter field, and thus circumventing the arduous task of explicitly tracking a moving boundary. Using this approach, the moving sediment boundary in our case is represented with a diffuse boundary (with a very small interface thickness compared to the height of the sediment domain), and now its movement is dictated by the movement of a structural order parameter field, θ.

4.1 Order parameter based representation of the sedimentary domain

In our proposed treatment, we first convert an open system with an evolving boundary into a closed system. The closed system dimensions are set by the maximum sedimentary domain height that can potentially be achieved during the time duration of sedimentation considered in a particular Initial Boundary Value Problem. The porous sediment region and the top boundary is then remodelled as a porous region, diffuse interface region, and a fictitious region that represents the empty space for accommodating potential growth of the sediment height, as depicted in Figure 1. The three regions are distinguished using an order parameter θ. For a known sediment deposition velocity $\boldsymbol{V}_0$, at an instant of time $\tilde{t} = t^{'}$, we know the location of the moving interface to be at a height of $\tilde{\boldsymbol{V}}_0 t^{'}$ from the base. The order parameter, θ, is defined such that it takes a value of 1.0 in the sediment region and a value of 0.0 in the fictitious region. The interface between the two regions is then determined by a θ value of 0.5. Figure 1 shows this spatial variation of the order parameter in relation to the compaction of the sediment.

A unique aspect of the phase field representation of the sedimentary domain proposed in this work is that the order parameter, θ, is explicitly defined as a function of time and sediment growth velocity, and is not solved using a separate first-order-in-time parabolic partial differential equation, as is commonly the case with the widely used Allen-Cahn or Cahn-Hilliard formulations [25, 26]. However, we do consider an interface parameter, λ, which controls the non-dimensional interface thickness of the phase field diffuse interface. As defined, a larger value of λ implies smaller interface thickness and thus a sharp transition of θ from 0.0 to 1.0. The definition of the order parameter we propose is as follows,

$$\theta = \frac{1}{2}\left(1 + \frac{e^{n} - e^{-n}}{e^{n} + e^{-n}}\right) \tag{11}$$

$$\text{where} \quad n = \lambda(\boldsymbol{V}_0 t - \tilde{y})$$

here, $\boldsymbol{V}_0$ is the magnitude of the sediment deposition velocity, so the product $\boldsymbol{V}_0 t$ gives the current sediment height at any time instance, t. Now, we non-dimensionalize the governing equations in Equations 8, 9, and 10 to arrive at the following governing equations that incorporate the phase-field order parameter, θ:

Preprints (www.preprints.org) | NOT PEER-REVIEWED | Posted: 6 December 2022 doi:10.20944/preprints202212.0093.v1

$$\frac{D\tilde{\phi}}{D\tilde{t}} = \theta(\alpha - \tilde{\phi})\tilde{\boldsymbol{\nabla}} \cdot \tilde{\boldsymbol{V}}_s \tag{12}$$

$$\tilde{\boldsymbol{V}}_s = -\tilde{\phi}^3\left(\frac{\partial \tilde{P}_e}{\partial \tilde{\boldsymbol{y}}} + \mathbf{1}\right) \tag{13}$$

$$\tilde{\phi}\tilde{\beta}\frac{D\tilde{P}_e}{D\tilde{t}} = -\theta\frac{\tilde{\phi}}{\tilde{\eta}}\tilde{P}_e - \theta\tilde{\boldsymbol{\nabla}} \cdot \tilde{\boldsymbol{V}}_s \tag{14}$$

Lastly, the general boundary conditions considered in this model are as follows: at the bottom end of the sediment region we specify $\tilde{\boldsymbol{V}}_s = 0$, and at the top of the fictitious domain, $\tilde{P}_e = 0$, $\tilde{\phi} = 1$. The initial conditions of the primal fields are taken to be $\tilde{\phi}(\tilde{\boldsymbol{y}}, 0) = 1.0$, $\tilde{P}_e(\tilde{\boldsymbol{y}}, 0) = 0.0$ and $\tilde{\boldsymbol{V}}_s(\tilde{\boldsymbol{y}}, 0) = 0$ everywhere in the numerical domain.

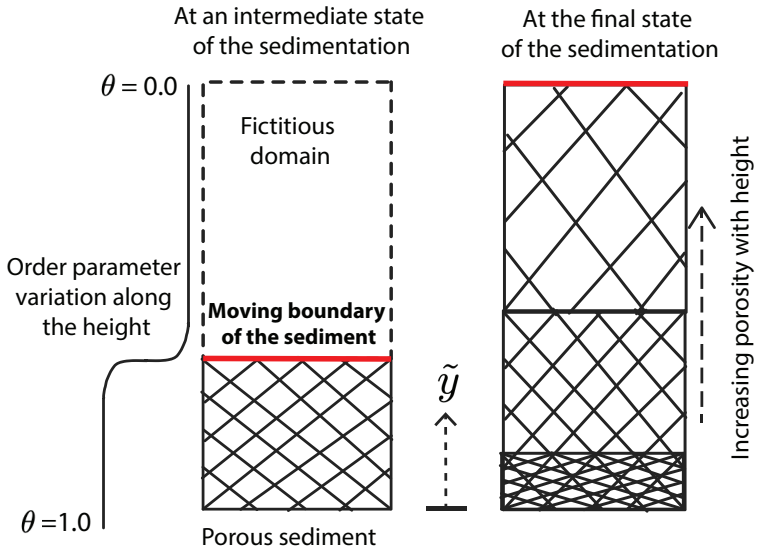

Figure 1: Schematic showing order parameter distinguishing the sediment region, the moving interface and the fictitious region at an intermediate time instance of the sediment deposition process. The red solid line is the moving interface that denotes the current height of the sediment. The zone bounded by the dashed line represents the fictitious region that is above the current moving interface. The right figure is a schematic representation of the porosity variation along the depth due to compaction, with the higher density of hatch-lines representing lower porosity.

In the fictitious domain, since θ is set to zero by construction, there is no change in the initial values of the porosity and the effective pressure, as $\frac{D\tilde{\phi}}{D\tilde{t}} = 0$ and $\frac{\partial \tilde{P}_e}{\partial \tilde{t}} = 0$. As a result of this, $\tilde{\phi}$ and $\tilde{P}_e$ do not evolve in the fictitious region. Thus, the boundary conditions at the interface are trivially satisfied.

Preprints (www.preprints.org) | NOT PEER-REVIEWED | Posted: 6 December 2022 doi:10.20944/preprints202212.0093.v1

4.2 Weak formulation of the phase-field treatment

We now pose the above governing equations in their weak form. This formulation is used to solve these equations within a standard finite element framework. Find the primal fields $\{\tilde{\phi}, \tilde{\boldsymbol{V}}_s, \tilde{P}_e\}$, where,

$$\tilde{\phi} \in \mathscr{S}_{\tilde{\phi}}, \quad \mathscr{S}_{\tilde{\phi}} = \{\tilde{\phi} \mid \tilde{\phi} = \tilde{\phi}' \; \forall \; \mathbf{X} \in \Gamma^{\tilde{\phi}}\},$$

$$\tilde{\boldsymbol{V}}_s \in \mathscr{S}_{\tilde{\boldsymbol{V}}_s}, \quad \mathscr{S}_{\tilde{\boldsymbol{V}}_s} = \{\tilde{\boldsymbol{V}}_s \mid \tilde{\boldsymbol{V}}_s = \tilde{\boldsymbol{V}}_s' \; \forall \; \mathbf{X} \in \Gamma^{\tilde{\boldsymbol{V}}_s}\},$$

$$\tilde{P}_e \in \mathscr{S}_{\tilde{P}_e}, \quad \mathscr{S}_{\tilde{P}_e} = \{\tilde{P}_e \mid \tilde{P}_e = \tilde{P}_e' \; \forall \; \mathbf{X} \in \Gamma^{\tilde{P}_e}\}$$

such that,

$$\forall \; w_{\tilde{\phi}} \in \mathscr{V}_{\tilde{\phi}}, \quad \mathscr{V}_{\tilde{\phi}} = \{w_{\tilde{\phi}} \mid w_{\tilde{\phi}} = 0 \; \forall \; \mathbf{X} \in \Gamma^{\tilde{\phi}}\},$$

$$\forall \; \boldsymbol{w}_{\tilde{\boldsymbol{V}}_s} \in \mathscr{V}_{\tilde{\boldsymbol{V}}_s}, \quad \mathscr{V}_{\tilde{\boldsymbol{V}}_s} = \{\boldsymbol{w}_{\tilde{\boldsymbol{V}}_s} \mid \boldsymbol{w}_{\tilde{\boldsymbol{V}}_s} = \mathbf{0} \; \forall \; \mathbf{X} \in \Gamma^{\tilde{\boldsymbol{V}}_s}\},$$

$$\forall \; w_{\tilde{P}_e} \in \mathscr{V}_{\tilde{P}_e}, \quad \mathscr{V}_{\tilde{P}_e} = \{w_{\tilde{P}_e} \mid w_{\tilde{P}_e} = 0 \; \forall \; \mathbf{X} \in \Gamma^{\tilde{P}_e}\}$$

we have,

$$\int_{\Omega} w_{\tilde{\phi}} \left(\frac{D\tilde{\phi}}{D\tilde{t}} - \theta(\alpha - \tilde{\phi}) \tilde{\boldsymbol{\nabla}} \cdot \tilde{\boldsymbol{V}}_s \right) dV = 0 \tag{15}$$

$$\int_{\Omega} \boldsymbol{w}_{\tilde{\boldsymbol{V}}_s} \cdot \left(\tilde{\boldsymbol{V}}_s + \tilde{\phi}^3 \left(\frac{\partial \tilde{P}_e}{\partial \tilde{\boldsymbol{y}}} + \mathbf{1} \right) \right) dV = 0 \tag{16}$$

$$\int_{\Omega} w_{\tilde{P}_e} \left(\tilde{\phi} \tilde{\beta} \frac{D\tilde{P}_e}{D\tilde{t}} + \theta \frac{\tilde{\phi}}{\tilde{\eta}} \tilde{P}_e + \theta \tilde{\boldsymbol{\nabla}} \cdot \tilde{\boldsymbol{V}}_s \right) dV = 0 \tag{17}$$

The order parameter, θ, is explicitly determined at each point using Equation 11.

4.3 Computational implementation

The phase-field formulation presented above is numerically solved using the Finite Element Method (FEM). The computational implementation is in an in-house, C++ programing language based, parallel code framework for finite element modeling. Standard FEM constructs are adopted, and for all the simulations presented in this work, either a Linear or Quadratic Lagrange basis is used. The time-stepping is based on the implicit backward Euler scheme.

Preprints (www.preprints.org) | NOT PEER-REVIEWED | Posted: 6 December 2022 doi:10.20944/preprints202212.0093.v1

This framework is build on top of the deal.II open source finite element library [30]. Following the standard practise in our group to release all research codes as open source [31, 32, 33, 34, 35], the complete code base for this work is made available to the wider research community as an open-source library [36].

5 Numerical results

In this section, we present the numerical studies done using the phase-field model represented by the Equations 15-17. This section is divided into three subsections. In Subsection 5.1, we present the comparison of our phase-field model of sediment compaction with the published results obtained from conventional numerical models with moving boundaries. Then, we present a comparison of the phase field model results with a reduced order problem that models compaction, but with a fixed sediment height, as this problem has an analytical solution. In Subsection 5.2, we present a sediment compaction problem in a two-dimensional geometry. Finally, in Subsections 5.3 and 5.4, we extensively demonstrate the application of our numerical method to model realistic geological conditions, especially the impact of the material state and the impact of material properties on the sediment compaction.

5.1 Validation studies of sediment compaction in 1D

For the phase-field model of sediment compaction to be used for studying geologically relevant open boundary compaction problems, it needs to be validated against known analytical and numerical results from the literature. For this purpose, we chose two types of sediment compaction problems that are classical, and have varying complexity. The first problem is the moving boundary sediment compaction model we developed rigorously in Section 3. For this problem, we use the phase-field model of sediment compaction in a one-dimensional setting and compare it with results in the literature obtained using conventional numerical methods with an evolving domain. This is covered in Subsection 5.1.1. We then remove the complexity of the moving boundary and viscous behavior of sediment compaction. This simplified representation is the classical poroelastic soil compaction model which was originally presented by Terzaghi [37]. We solve this model of sediment compaction of fixed height using our phase-field framework and present the comparison with the known 1D analytical solution in Subsection 5.1.2.

5.1.1 1D poro-viscoelastic compaction with varying sediment height

The physical phenomenon evident in sediment compaction is the expulsion of fluid from the pores. This expulsion is driven by the action of the effective pressure on the porous sediment. Further, we observe the sediment deformation due to changes in the pore volume, porosity, or void ratio. The open boundary nature of this compaction problem is due to the continuous deposition of the

Preprints (www.preprints.org) | NOT PEER-REVIEWED | Posted: 6 December 2022 doi:10.20944/preprints202212.0093.v1

sediment from the top and this increases the overburden pressure. Denoting this model as the higher-order representation, it is pictorially represented in the first half of Figure 3. We compared the phase-field model of the sediment compaction problem with the results published in the literature. The phase-field representation of this model is depicted in Figure 1. We particularly chose the popular moving boundary sediment compaction studies presented by Suetnova and Vasseur [18]. To the best of our knowledge, published results in this study are obtained by changing the computational domain as the height of the sediment grows. We refer to this method of solving the compaction problem with the varying height as the conventional model. Figure 2 shows results obtained from our phase-field model and the corresponding results from the literature for the conventional model. Figures 2a and 2b shows the normalized height $\tilde{\boldsymbol{y}}/\tilde{H}$ on the y-axis plotted with the non-dimensional porosity $\tilde{\phi}$ and the pore fluid pressure $\tilde{P}_f$ on the x-axis respectively. Each solid curve represents time instants at which $\tilde{\boldsymbol{y}}/\tilde{H}$ vs $\tilde{\phi}$ (or $\tilde{P}_f$) was obtained. As seen in the Figures 2a and 2b, the variation of $\tilde{\phi}$ and $\tilde{P}_f$ with $\boldsymbol{y'}$ follows the pattern closely with the reported values from the literature [18].

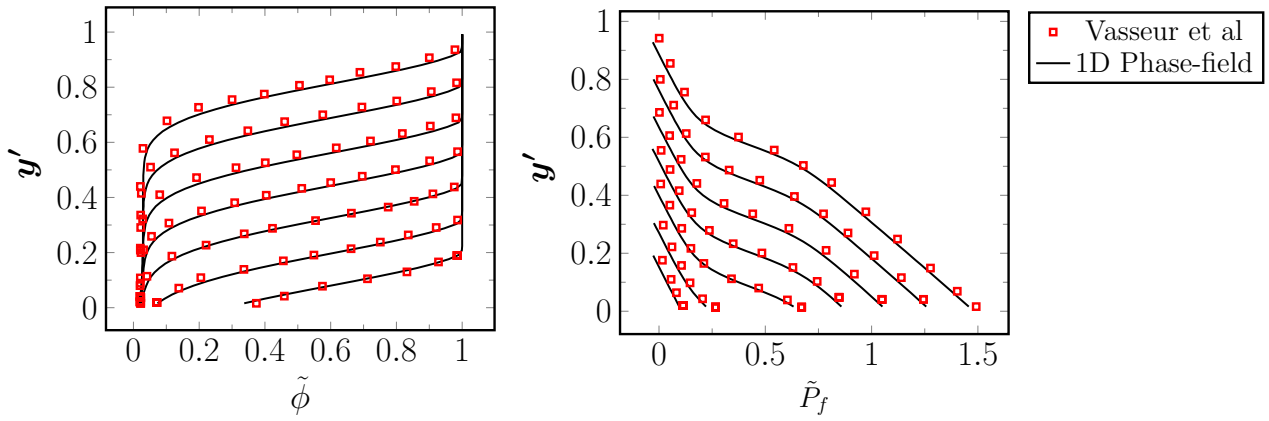

(a) Sediment porosity (b) Pore fluid pressure

Figure 2: (2a) Sediment Porosity ($\tilde{\phi} = \frac{\phi}{\phi_0}$) and the (2b) pore fluid pressure $\left(\tilde{P}_f = \tilde{P}_{solid} - \tilde{P}_e\right)$ with the distance from the base ($\boldsymbol{y'} = \frac{\boldsymbol{V_0}\tilde{t}}{H}$) at time instant $\tilde{t} = 1.14$, 1.82, 2.57, 3.25, 3.94, 4.68, and 5.4. Non-dimensional phase-field model parameters : mesh points 1000, time step $\Delta t = 1.0 \times 10^{-3}$, final height $\tilde{H} = 0.93$, $\alpha = 0.1$, $\beta = 7.14 \times 10^{-3}$, $V_0 = 0.16$, $\tilde{\eta} = 1$ and quadratic FE basis.

5.1.2 1D poroelastic compaction with fixed sediment height

In the previous subsection, we briefly described the sediment compaction due to the overburden pressure exerted by the deposited sediment resulting in the varying height of the sediment. We then solved this problem in a one-dimensional setting using our phase-field model and obtained an excellent comparison with the results presented in the published literature.

 doi:10.20944/preprints202212.0093.v1

In the reduced order representation of the sediment compaction (or soil consolidation), the sediment column is unchanged as there is no deposition of the sediment. The overburden pressure in the higher-order model is replaced with the application of the surcharge pressure at the top of the sediment. This surcharge pressure is the excess pressure in the fluid above its hydrostatic pressure. Further, the compaction of the sediment is modeled using a purely poroelastic constitutive law as opposed to poro-viscoelastic law in the higher-order model. The increase in the pressure on the porous sediment after the application of the surcharge pressure is entirely borne by the fluid in the pores at the start. With time, the sudden increase in the excess fluid pressure starts diffusing. The governing equation of the excess pressure diffusion is similar to parabolic partial differential equations of unsteady heat diffusion which are extensively studied. As a result analytical solutions for the excess fluid pressure diffusion are well known and various types of sediment compaction cases were covered by Terzaghi [37]. The continuous diffusion of the excess fluid pressure results in the continuous rise in the effective pressure of the sediment. The rise of the effective pressure causes sediment compaction. Since the solid and fluid are incompressible in porous sediment, the compaction is manifested in the purging or escape of the fluid from the loose sediments. The extent of compaction is also related to the permeability of the sediment. The reduced order is pictorially represented in the second half of Figure 3.

In the reduced order model, the sediment is confined to a column whose width is irrelevant in the one-dimensional setting. Along the width, the variation of the field variables is neglected. The height of the sediment column is taken as constant and denoted by H. At time t=0, a surcharge pressure P_0 is applied on the top surface. The system is then allowed to settle under the application of the surcharge pressure. This settlement process involves a change in the volume of the sediment, expulsion of the fluid from the voids, and the consolidation of the loose sediment. We allow the temporal variation of the porosity. Sediment permeability and material properties of the solid and fluid are taken as constant. The bottom surface is impervious and does not allow fluid from the pores to escape. At the top surface, effective pressure is taken to be zero and fluid can drain from this surface. This reduced order model of sediment compaction is modeled in our phase-field framework, but with a non-evolving order parameter distribution to mimic the fixed sediment height, and compared with the analytical solution given by Terzaghi [37]. The solution from the finite element (FE) model is in excellent agreement with the known analytical solution from the literature, as can be seen in Figure 4.

5.2 Phase-field model of compaction on a 2D geometry

In this section, we demonstrate the capability of the model to simulate sedimentation and compaction in a 2D geometry. The nature of sediment compaction we are dealing with in this paper is along the direction of gravity. Thus, the solid or fluid velocity, sediment porosity, and pore pressure variation can be seen only along the direction of gravity. Figure 5 shows two-dimensional sediment

Preprints (www.preprints.org) | NOT PEER-REVIEWED | Posted: 6 December 2022 doi:10.20944/preprints202212.0093.v1

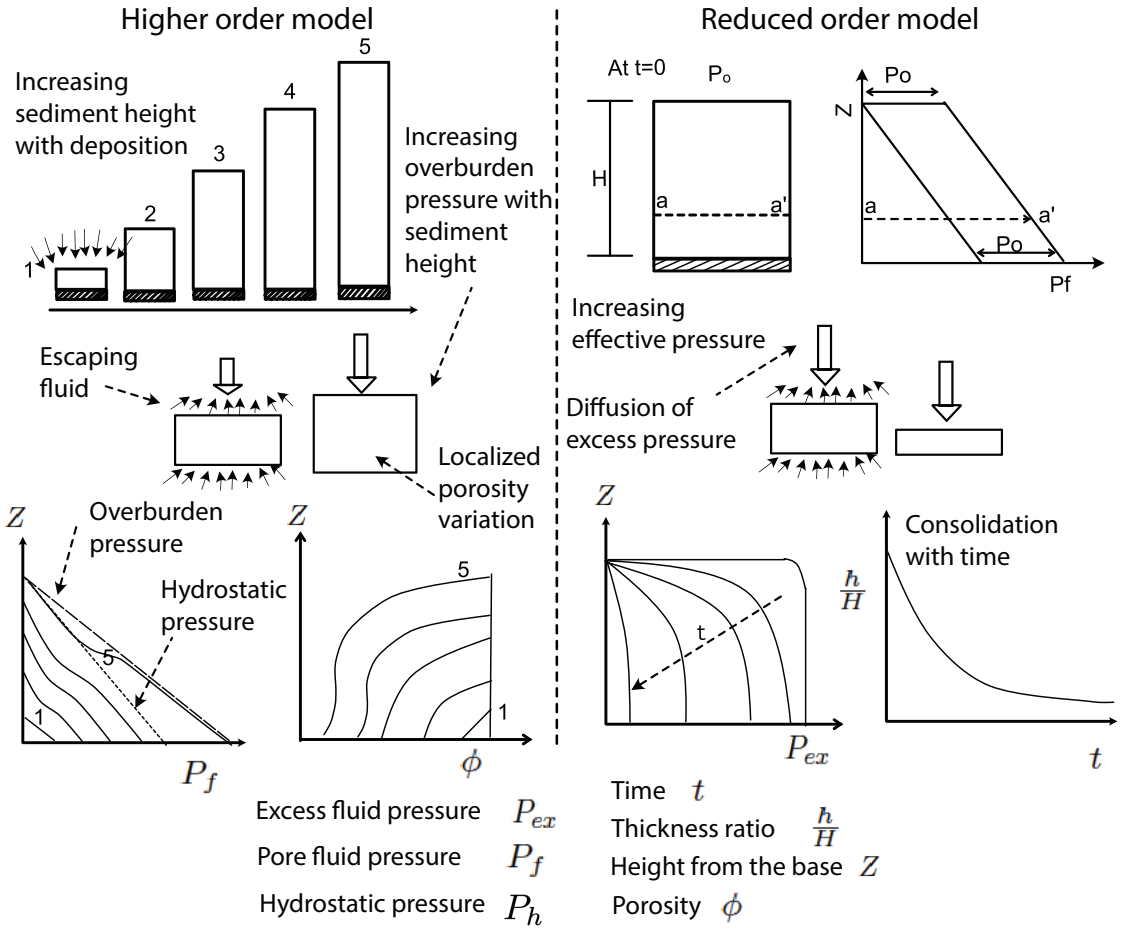

Figure 3: Schematic showing the higher order model and the reduced order model of sediment compaction.

column and the porosity $\tilde{\phi}$ and order parameter θ with the column height. The order parameter contours clearly distinguish the porous sediment (in red), interface region (in green), and the fictitious region (in blue). With time, the interface moves along the Z direction, representing the deposition of the sediment. The porosity, $\tilde{\phi}$, is overlaid as a black solid line. There is no variation of porosity perpendicular to the Z direction. Porosity takes a value of one in the fictitious region, and varies non-linearly in the bulk sediment region. It is nearly constant in the interface region and decreases as we move along the depth in the sediment region.

5.3 Investigation of the effect of the material state on the compaction process

The phase-field model of compaction was successfully validated with the published results obtained using the conventional models of compaction in Subsection 5.1.1. The scalability of the phase-field model of compaction to 2D (and, if needed, to 3D) was shown in Subsection 5.2. In this subsection,

Preprints (www.preprints.org) | NOT PEER-REVIEWED | Posted: 6 December 2022 doi:10.20944/preprints202212.0093.v1

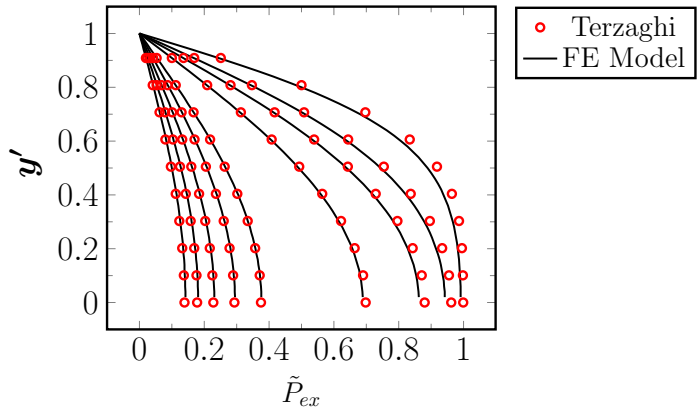

Figure 4: One dimensional sediment compaction problem with excess hydrostatic pressure at $\tilde{t} = 0.05, 0.1, 0.15, 0.25, 0.5, 0.6, 0.7, 0.8, 0.9$ using analytical solution from [37] and FE model for $\tilde{T} = \frac{C_v}{H^2} = 1.0$, $H = 1.0$, $\tilde{P}_0 = 1.0$, $\tilde{\Delta t} = 0.01$, $\tilde{\Delta x} = 0.01$, and linear FE basis.

we demonstrate the applicability of the model by simulating the different compaction scenarios, interpret the results, and make connections to the classical understanding of the compaction process, where needed. This subsection specifically deals with understanding the effect of change in the material state and how it impacts the sediment porosity and the pore fluid pressure. The material state can be referred to as the deposition rate of the water-logged sediment or the characteristic porosity of the sediment material. In our model, the material state is associated with the interface moving velocity $\tilde{\boldsymbol{V}}_0$ or the initial porosity of the system $\alpha = \frac{1}{\phi_0}$.

Parameter	Value	Unit
Final height H	4×10^3	m
Fluid viscosity μ	2.6×10^{-4}	Pa-s
Solid viscosity η	5.0×10^{22}	Pa-s
Solid density ρ_s	2.65×10^3	$\frac{kg}{s}$
Liquid density ρ_l	1.0×10^3	$\frac{kg}{s}$
Permeability k_0	1.0×10^{-16}	m^2
Compressibility β	1.0×10^{-9}	$\frac{1}{Pa}$
Deposition rate $\boldsymbol{V}_0$	1.0×10^{-11}	$\frac{m}{s}$
Characteristic ϕ_0	1.0×10^{-1}	Constant
Characteristic η_0	5.0×10^{20}	Pa-s
Power exponent m	3.0×10^0	Constant
Numerical factor d	1.0×10^0	Constant

Table 2: Material properties and characteristics parameters of the water-logged sediments [18]

Preprints (www.preprints.org) | NOT PEER-REVIEWED | Posted: 6 December 2022 doi:10.20944/preprints202212.0093.v1

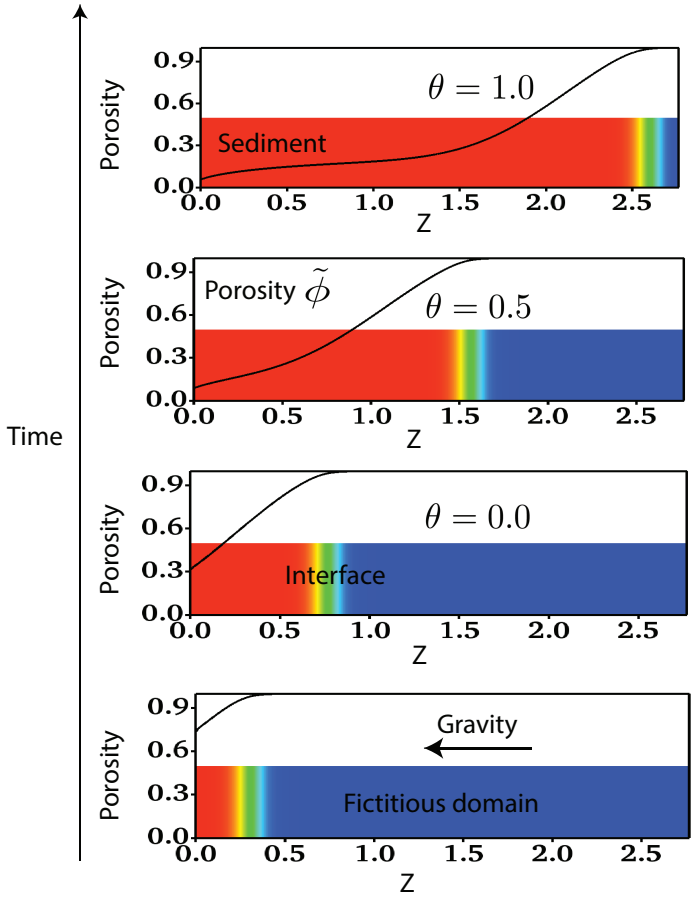

Figure 5: Contours representing the porous region (in red), the diffuse interface (in green), and the fictitious region (in blue). Gravity acts along the Z-axis from right to left. Solid black line represents normalized porosity, $\tilde{\phi}$, variation along the Z-axis. From bottom to top, the simulation time is $\tilde{t} = 0.2, 0.7, 1.2$ and 1.7. Uniform mesh with $\Delta x = 0.016$, and time step $\Delta\tilde{t} = 10^{-3}$, Non-dimensional domain of size 2.77×0.5, $\alpha = 2.5$, $\tilde{\beta} = 2.27 \times 10^{-3}$, $\tilde{\eta} = 1$, and $\lambda = 10.0$

5.3.1 Impact of the sediment deposition rate

For this study, we chose sediment properties given in Table 2. To be specific, we simulated four scenarios of the sediment compaction where we varied the water-logged sediment deposition rate by changing the interface moving velocity $\boldsymbol{V}_0 = 5.0 \times 10^{-12}, 1.0 \times 10^{-11}, 5.0 \times 10^{-11}, 1.0 \times 10^{-10}\ \frac{m}{s}$. In the course of sediment deposition, when the column height $H = 4000$ m is attained, we stopped the simulation. It is useful to note that final height is achieved earlier when $\boldsymbol{V}_0$ is greater. Thus the four scenarios shown in the Figure 6 refer to different time instant at which distribution of ϕ and P_f is reported. We showed the variation of absolute porosity (ϕ) and the pore fluid pressure (P_f) with the height from the base of the column in the Figures 6a and 6b. The overburden pressure due to the weight of the sediment and the hydrostatic fluid pressure is also shown in the Figure 6b.

Preprints (www.preprints.org) | NOT PEER-REVIEWED | Posted: 6 December 2022 doi:10.20944/preprints202212.0093.v1

The Figure 6a shows the variation of porosity at a height from the base for four cases of the V_0. The porosity at the top of the sediment column is always chosen to be $\phi_0 = 0.1$. This indicates the volume of the sediment is not changed in the absence of deposited sediments. As we move downwards in the direction of the base, the porosity reduces non-linearly for all cases of $\boldsymbol{V}_0$. Since the solid section of the sediment and the fluid are incompressible, the compaction of the sediment is manifested as the drop in the porosity, ϕ. Simultaneously, the fluid occupying the volume inside the pores is squeezed out in the process of compaction. The largest drop in the porosity is seen for the case with the slower sediment deposition rate. This variation is captured at the time instant of $t = 8.0 \times 10^{14} s$. In the case with the largest deposition rate, we presented the data at the time instant of $t = 4.0 \times 10^{13} s$ so compaction takes place to a lesser extent.

Figure 6b shows the variation of pore fluid pressure, overburden pressure, and the hydrostatic pressure with the height from the base of the sediment column. The pore pressure is zero near the surface of the basin which is the top of the sediment column. As we move towards the base of the column, the P_f increases for all four cases of $\boldsymbol{V}_0$. At any time instant and height from the base, the value of P_f always lies between the hydrostatic and the overburden pressure value. The pore pressure of the fluid P_f deviates from the hydrostatic value and reaches an abnormally high value closer to the overburden pressure. For $\boldsymbol{V}_0 = 5 \times 10^{-12}$ and 1×10^{-11} m/s, the drop in the ϕ is higher as compared to rest of the two cases. The P_f starts from zero at the top surface with a pressure gradient equal to the hydrostatic gradient. As we move down, the P_f increases in a non-linear fashion until porosity is drastically reduced at which point, P_f increases with pressure gradient equal to that of overburden gradient. For the case, $\boldsymbol{V}_0 = 1.0 \times 10^{-10} m/s$, the drop in the porosity is lowest and thus the fluid in the pores does not experience the maximum possible compressive force resulting in the pore pressure value less than that for the case for $\boldsymbol{V}_0 = 5.0 \times 10^{-12} m/s$ at the lower end of the sediment column.

5.3.2 Impact of the initial porosity of the water-logged sediment

In this subsection, we understand how the overall compaction process is influenced in the light of changing the characteristics porosity ϕ_0. In our model, we chose initial porosity value to be $\phi = \phi_0$ (or $\tilde{\phi} = 1.0$). The effect on the compaction process is then studied by observing the variation of porosity (ϕ) and pore pressure (P_f) with height as shown in the Figure 7. We chose material properties and the characteristics quantities from the Table 2. For this particular study, we varied $\phi = 0.05, 0.1, 0.2$ and 0.4. As the $V_0 = 1.0 \times 10^{-11} m/s$ is same for all four cases, we stopped the simulation when $t = 4 \times 10^{14}$s and the final height $H = 4000$m is attained. Figure 7a shows the variation of ϕ with the height from the base of the sediment for different ϕ_0 values. It is understood that the $\phi = \phi_0$ near the basin surface at 4000 m. If we move downward the compaction of the sediment is understood by the decreasing value of ϕ. The maximum relative percentage change near base is found to be $94\%, 97\%, 99\%$ and 99% for the case $\phi_0 = 0.05, 0.1, 0.2, 0.4$ respectively.

Preprints (www.preprints.org) | NOT PEER-REVIEWED | Posted: 6 December 2022 doi:10.20944/preprints202212.0093.v1

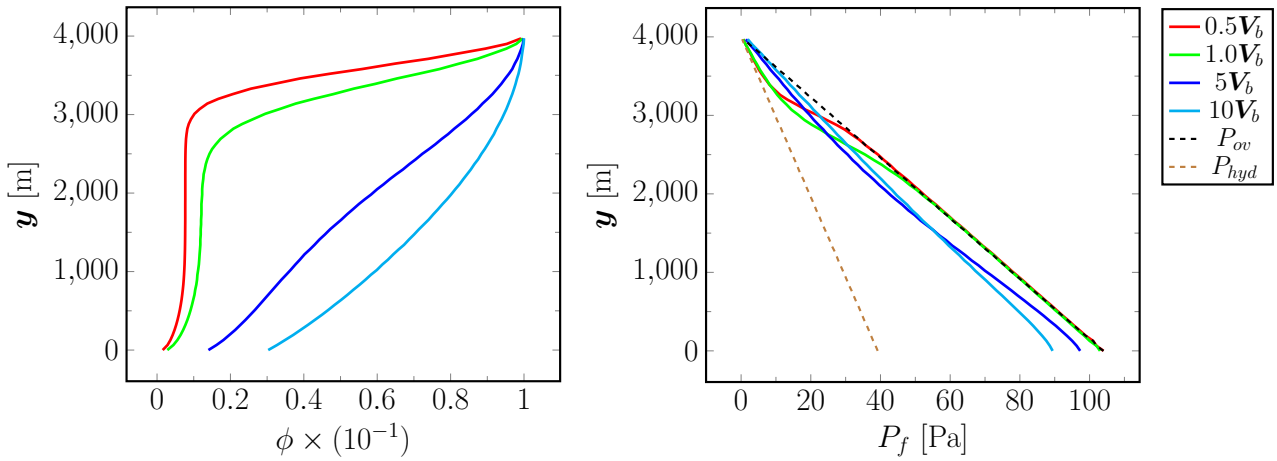

(a) Sediment porosity (b) Pore pressure

Figure 6: Variation of a porosity ϕ and the pore fluid pressure P_f as function of height $\boldsymbol{y}$ for different deposition rate $\boldsymbol{V}_0$ such as $\boldsymbol{V}_0/\boldsymbol{V}_b = 0.5, 1.0, 5.0, 10.0$ where $\boldsymbol{V}_b = 1.0 \times 10^{-11} m/s$. The equations were solved in a non-dimensional framework with a time step size $\Delta t = 1.0 \times 10^{-3}$, $\lambda = 200$ and quadratic FE basis for all four cases. Subscript 'b' refers to the base case here and in the subsequent figures. $P_{ov} = \rho_s \boldsymbol{g}(H - \boldsymbol{y})$ is the overburden pressure, and $P_{hyd} = \rho_l \boldsymbol{g}(H - \boldsymbol{y})$ is the hydrostatic pressure in this and the subsequent figures.

We can then conclude that the maximum possible compaction have taken place in the sediment in all the four cases for the chosen set of parameters.

Figure 7b shows the pore fluid pressure P_f with a height from the base. As observed previously in Figure 6b, the pore fluid pressure P_f is zero near the basin surface at 4000m for all four cases of ϕ_0. The P_f increases non-linearly as we move away from the top of the sediment column. However, near the base of the sediment column, the non-linear variation of P_f changes to linear variation with a constant slope equal to that of the overburden pressure gradient. Since the absolute porosity is comparable from base to height of 3000m, the pores fluid in all four the cases experiences similar overburden pressure resulting in the similar pore fluid pressure.

5.4 Investigation of the effect of the material properties on the compaction process

In the Subsection 5.3, we understood the extent of the compaction process brought out by changing the water-logged sediment deposition rate $\boldsymbol{V}_0$ and the characteristics porosity ϕ_0. In this subsection, we use the phase-field model to inspect how the material properties of the sediment impact the compaction of the sediment. Specifically, we check how the pore compressibility β, solid viscosity η, and the sediment permeability k_0 affects the overall compaction process. In the forthcoming

Preprints (www.preprints.org) | NOT PEER-REVIEWED | Posted: 6 December 2022 doi:10.20944/preprints202212.0093.v1

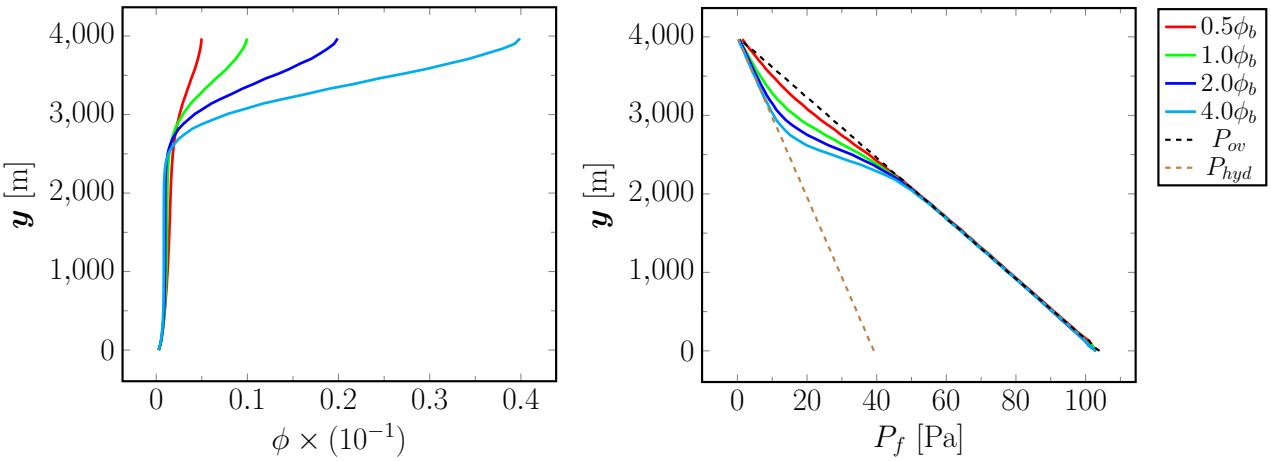

(a) Sediment porosity (b) Pore pressure

Figure 7: Variation of a porosity ϕ and the pore fluid pressure P_f as function of height $\boldsymbol{y}$ for different initial porosity $\frac{\phi_0}{\phi_b} = 0.5, 1.0, 2.0, 4.0$ where $\phi_b = 0.1$. The equations were solved in a non-dimensional framework with a time step size $\Delta t = 1.0 \times 10^{-3}$, $\lambda = 200$ and quadratic FE basis for all four cases. P_{ov} is the overburden pressure, and P_{hyd} is the hydrostatic pressure.

analysis, we varied one material properties at a time keeping everything else fixed. We then plotted the sediment porosity and pore fluid pressure when the final height H=4000m is attained.

5.4.1 Impact of the pore compressibility, β, of the sediment

In this analysis, we simulated four scenarios of the compaction process with the different pore compressibility β value. We kept the other material properties fixed as given in the Table 2. The pore compressibility were taken as $\beta = 10^{-10}, 10^{-9}, 10^{-8}, 10^{-7}\ Pa^{-1}$. The Figure 8a-8b shows the variation of the sediment porosity ϕ and the pore pressure P_f with the height from the base. The maximum percent change in the porosity at the bottom end of the sediment is 97.3%, 97.2%, 97.1% and 96.8% for the four cases of β respectively. It can be inferred that the large change in the pore compressibility parameter brings about an identical change in the porosity distribution. Further, the fluid pressure distribution is similar in all four cases. It is then implied that the sediment material when subjected to the loading is not sensitive to the change in the pore compressibility. Sediment material is thus behaving less elastically as learned from this analysis.

5.4.2 Impact of the solid viscosity, η, of the sediment

For the viscoelastic constitutive model chosen, we studied the impact of the pore compressibility β on the compaction process in a parametric study carried out in the preceding subsection. In this subsection, we focus on the impact seen in the compaction process when the solid viscosity

Preprints (www.preprints.org) | NOT PEER-REVIEWED | Posted: 6 December 2022 doi:10.20944/preprints202212.0093.v1

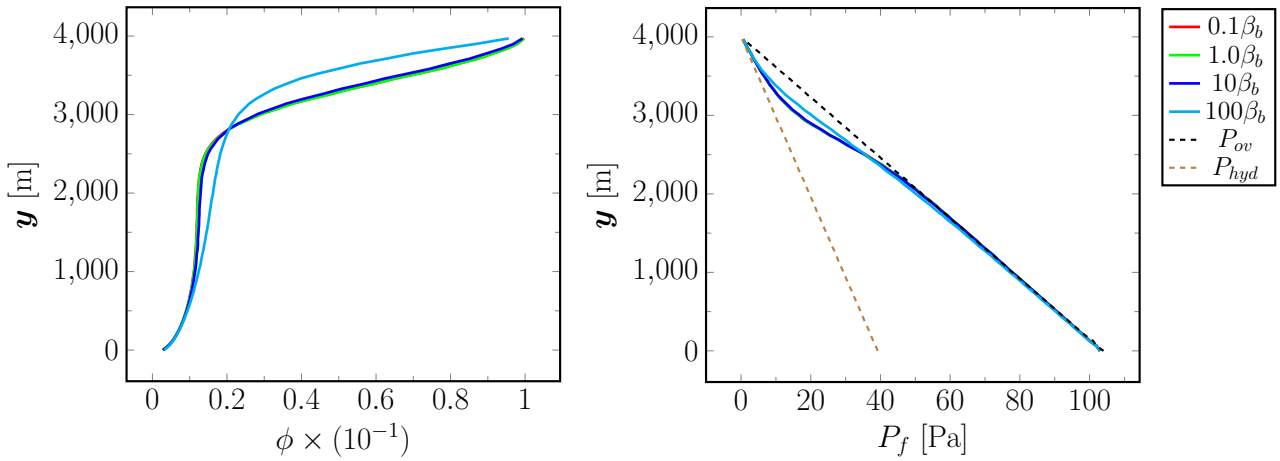

(a) Sediment porosity (b) Pore pressure

Figure 8: Variation of a porosity ϕ and the pore fluid pressure P_f as function of height $\boldsymbol{y}$ for different pore compressibility $\frac{\beta}{\beta_b} = 0.10, 1.0, 10.0, 100$ where $\beta_b = 1.0 \times 10^{-9} Pa^{-1}$. The equations were solved in a non-dimensional framework with a time step size $\Delta t = 1.0 \times 10^{-3}$, $\lambda = 200$ and quadratic FE basis for all four cases. P_{ov} is the overburden pressure, and P_{hyd} is the hydrostatic pressure.

value of the sediment is changed. For the current analysis, we fixed characteristic solid viscosity $\eta_0 = 5.0 \times 10^{20}$ Pa-s and varied solid viscosity $\eta = 1.0 \times 10^{20}, 5.0 \times 10^{20}, 2.5 \times 10^{21}$ and 1.25×10^{22} Pa-s. The rest of the parameters are kept the same as given in the Table 2. We plotted the porosity ϕ and the pore fluid P_f as a function of height from the base of the sediment in Figure 9. As seen in Figure 9a, the ϕ decreases as we go along the depth of the sediment for all four values of solid viscosity considered. The maximum percentage in the porosity at the base was found to be $98\%, 97\%, 64\%$ and 9% for solid viscosity of $\eta = 1.0 \times 10^{20}, 5.0 \times 10^{20}, 2.5 \times 10^{21}$, and 1.25×10^{22}. In the Figure 9a, the compaction of the sediment is most evident for the case of $\eta = 1.0 \times 10^{20}$ and $\eta = 5.0 \times 10^{20}$ Pa-s while the compaction is least in the case of $\eta = 1.25 \times 10^{22}$ Pa-s. The viscous response of the sediment is more pronounced in the viscoelastic constitutive model we used in this paper. The fluid pressure P_f as a function of distance from the base is shown in the Figure 9b. Like all the pressure plots, we can see the fluid pressure for all four cases lies between hydrostatic pressure and the overburden pressure. As we increase the solid viscosity, the compaction of the sediment is reduced with pores retaining more fluid. Thus, the fluid pressure moves away from the overburden value towards the hydrostatic value as there is less overall compaction.

Preprints (www.preprints.org) | NOT PEER-REVIEWED | Posted: 6 December 2022 doi:10.20944/preprints202212.0093.v1

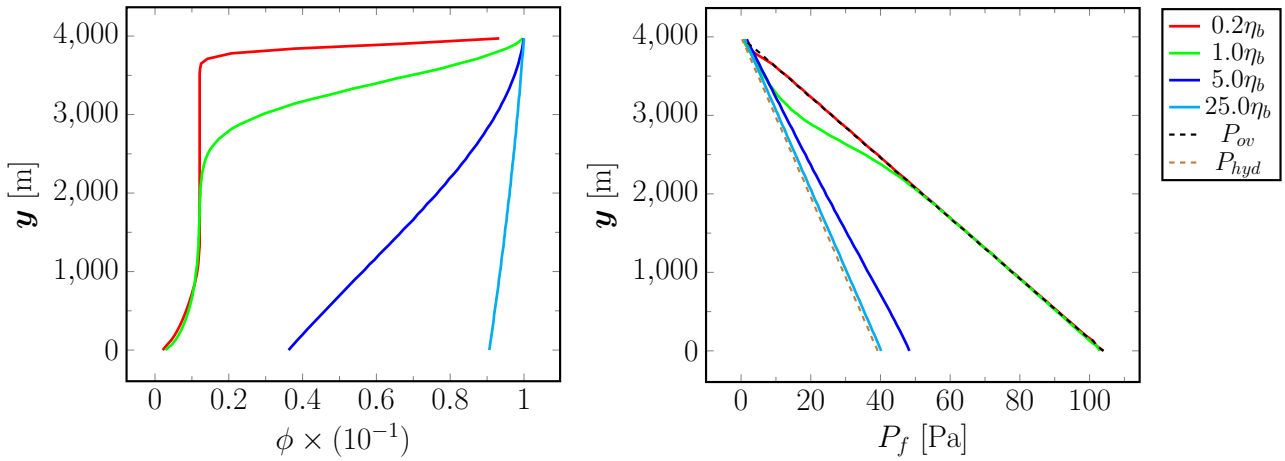

(a) Sediment porosity (b) Pore pressure

Figure 9: Variation of a porosity ϕ and the pore fluid pressure P_f as function of height $\boldsymbol{y}$ for different solid viscosity $\frac{\eta}{\eta_b} = 0.2, 1.0, 5, 25$ where $\eta_b = 5.0 \times 10^{20} Pa - s$. The equations were solved in a non-dimensional framework with a time step size $\Delta t = 1.0 \times 10^{-3}$, $\lambda = 200$ and quadratic FE basis for all four cases. P_{ov} is the overburden pressure, and P_{hyd} is the hydrostatic pressure.

5.4.3 Impact of the permeability coefficient, k_0, of the sediment

In this subsection, we gauge the impact the permeability coefficient k_0 has on the compaction process. In this analysis, we change the permeability coefficient $k_0 = 1.0 \times 10^{-17}, 1.0 \times 10^{-16}, 1.0 \times 10^{-15}$ and $1.0 \times 10^{-14} m^2$. The rest of the parameters are kept the same as given in the Table 2. Figure 10 shows the variation of porosity ϕ and fluid pressure P_f with the height from the base of the sediment column. The variation of the porosity and fluid pressure is as per the compaction process as discussed in the previous sections. In the Figure 10a, the porosity is seen as decreasing along with the depth for all cases of permeability considered. The compaction is more evident in the cases with a relatively higher k_0 values. Thus the sediments with higher permeability are compacted easily than the sediments with lower permeability. The permeability of a porous medium is associated with the amount of fluid passing through it. A high permeability porous system allows more fluid to pass through it as compared to the low permeability porous system. Thus, with better expulsion of fluid from the pores, the system compacts easily when the system is more permeable. In the Figure 10b, the pore fluid pressure for the smallest $k_0 = 0.1 k_b$ is closer to the overburden pressure. The pore fluid pressure for the other cases of k_0 is more closer to the hydrostatic pressure value near the top region of the sediment and approaches the abnormally high value closer to the overburden pressure near the bottom region of the sediment.

Preprints (www.preprints.org) | NOT PEER-REVIEWED | Posted: 6 December 2022 doi:10.20944/preprints202212.0093.v1

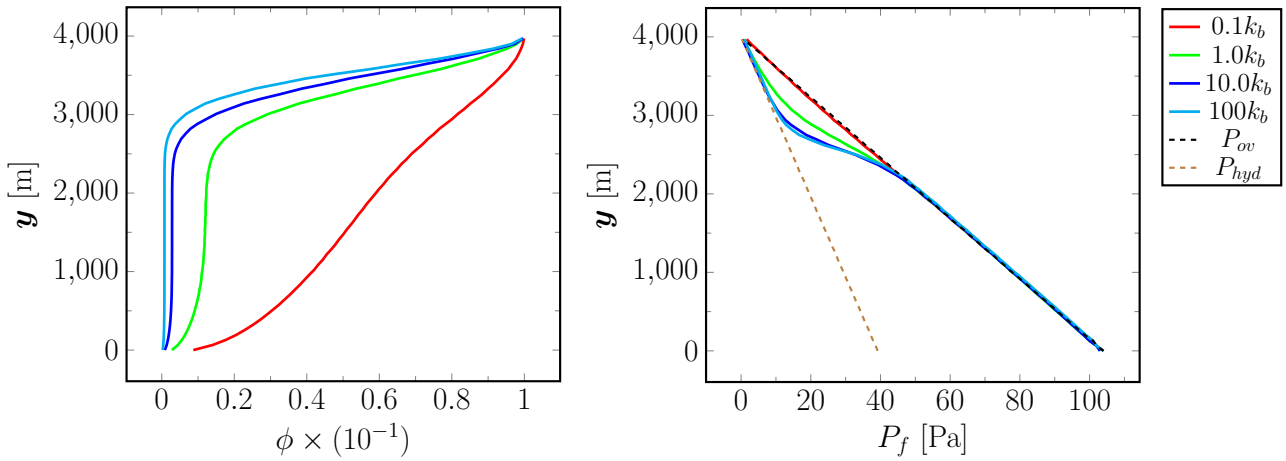

(a) Sediment porosity (b) Pore pressure

Figure 10: Variation of a porosity ϕ and the pore fluid pressure P_f as a function of height $\boldsymbol{y}$ for different permeability $\frac{k}{k_b} = 0.1, 1.0, 10.0, 100$ where $k_b = 10^{-16} m^2$. The equations were solved in a non-dimensional framework with a time step size $\Delta t = 1.0 \times 10^{-3}$, $\lambda = 200$ and quadratic FE basis for all four cases. P_{ov} is the overburden pressure, and P_{hyd} is the hydrostatic pressure.

6 Conclusion

In this work, we solved the sediment compaction problem by proposing a novel phase-field treatment and its numerical implementation. The water-logged rock or soil sediments are deposited on the water basins over time and the increasing volume of the sediments starts to compact under their weight. The physics of this process is mathematically formulated to fit into a moving interface phase-field model where an order parameter can be used to evolve the moving boundary and the underlying sediment. The governing equations of the phase-field model are solved using a standard finite element framework, and the computational implementation is made available as an open source code. Validation studies were carried out wherein we first compare our novel phase-field model of compaction with the results obtained using traditional sediment models published in the literature. We also consider a reduced-order representation of the poroelastic sediment compaction process under the application of surcharge pressure and the fixed sediment column height. The solutions of the phase-field framework for the reduced-order model were in excellent agreement with the known analytical solution for this problem. Having validated our numerical method with the results in the literature and a known analytical solution, we then demonstrated the application of the phase-field approach to a two-dimensional case of sediment compaction.

The phase-field model of sediment compaction was then used to simulate sediment compaction phenomena under various conditions of geological interest. Particularly, we look at the extent of pore pressure development, and the extent of the compaction under the initial material state and

 doi:10.20944/preprints202212.0093.v1

the material properties of the sediment. For studies on the effect of the initial material state, we investigated the effect for slower and faster sediment deposition rates, and at different characteristic porosities of the sediment. Further, we also conducted studies to understand the effect of change in the permeability, viscosity, and compressibility of the porous sediment on the pore pressure and porosity evolution.

The parametric studies reveal a good dependence between porosity ϕ and pore fluid pressure P_f, and thus follow existing conventional understanding. A high pore fluid pressure is associated with regions of low porosity. In the compaction of low permeability coefficient sediments, the expulsion of the fluid from the pores is restricted and pore pressures can increase. Further, sediment compaction is much more pronounced when the sediment deposition velocity and initial porosity are relatively smaller or if the permeability is higher. The deformation of the sediment is found to be less sensitive to the changes in the pore compressibility values when considering the viscoelastic constitutive law.

In conclusion, (1) The strong validation of our phase-field treatment results against predictions from traditional methods of solving open boundary sediment compaction problems, albeit without the limiting burden of evolving the numerical domain, and (2) The good agreement between the porosity dependence numerical studies on the fluid pore pressure for various cases and the existing conventional understanding, strongly support the applicability and scalability of this novel numerical framework to model more advanced sediment compaction problems and geometries.

Acknowledgement

The authors are very grateful to Prof. Hiroki Sone (Geological Engineering and Department of Civil and Environment Engineering, University of Wisconsin-Madison) for introducing us to this problem of sedimentary compaction, for providing constant technical guidance and encouragement for the development of the numerical model presented in this work and for feedback on this manuscript. This work is part of our broader collaboration with Prof. Hiroki Sone's research group on modeling sediments and rock mechanics.

Declarations

Conflict of interest: The authors declare that they have no conflict of interest.

References

[1] Birger Rasmussen. Radiometric dating of sedimentary rocks: the application of diagenetic xenotime geochronology. *Earth-Science Reviews*, 68(3-4):197–243, 2005.

 doi:10.20944/preprints202212.0093.v1

[2] Troyee Dasgupta and Soumyajit Mukherjee. *Sediment compaction and applications in petroleum geoscience*. Springer, 2020.

[3] Florent Brenguier, Michel Campillo, Céline Hadziioannou, Nikolai M Shapiro, Robert M Nadeau, and Éric Larose. Postseismic relaxation along the san andreas fault at parkfield from continuous seismological observations. *science*, 321(5895):1478–1481, 2008.

[4] Matthew J Brain. Past, present and future perspectives of sediment compaction as a driver of relative sea level and coastal change. *Current Climate Change Reports*, 2(3):75–85, 2016.

[5] Karl von Terzaghi. Die berechnug der durchlassigkeit des tones aus dem verlauf der hydromechanischen spannungserscheinungen. *Sitzungsber. Akad. Wiss.(Wien). Math.-Naturwiss. Kl., Abt. Iia*, 132:125–138, 1923.

[6] Maurice A Biot. General theory of three-dimensional consolidation. *Journal of applied physics*, 12(2):155–164, 1941.

[7] Robert E Gibson. The progress of consolidation in a clay layer increasing in thickness with time. *Geotechnique*, 8(4):171–182, 1958.

[8] JD Bredehoeft and BB Hanshaw. On the maintenance of anomalous fluid pressures: I. thick sedimentary sequences. *Geological Society of America Bulletin*, 79(9):1097–1106, 1968.

[9] JE Smith. The dynamics of shale compaction and evolution of pore-fluid pressures. *Journal of the International Association for Mathematical Geology*, 3(3):239–263, 1971.

[10] DM Audet and AC Fowler. A mathematical model for compaction in sedimentary basins. *Geophysical Journal International*, 110(3):577–590, 1992.

[11] Andrew C Fowler and Xinshe Yang. Pressure solution and viscous compaction in sedimentary basins. *Journal of Geophysical Research: Solid Earth*, 104(B6):12989–12997, 1999.

[12] F Schneider, JL Potdevin, S Wolf, and I Faille. Mechanical and chemical compaction model for sedimentary basin simulators. *Tectonophysics*, 263(1-4):307–317, 1996.

[13] X-S Yang. Nonlinear viscoelastic compaction in sedimentary basins. *Nonlinear Processes in Geophysics*, 7(1/2):1–8, 2000.

[14] Craig M Bethke and Thomas F Corbet. Linear and nonlinear solutions for one-dimensional compaction flow in sedimentary basins. *Water Resources Research*, 24(3):461–467, 1988.

[15] Guo-Xiong Mei, Jian-Hua Yin, Jin-Min Zai, Zong-Ze Yin, Xiao-Li Ding, Guo-Fu Zhu, and Lok Man Chu. Consolidation analysis of a cross-anisotropic homogeneous elastic soil using a finite layer numerical method. *International Journal for Numerical and Analytical Methods in Geomechanics*, 28(2):111–129, 2004.

[16] Toyoaki Nogami, W Wang, and Jian-Guo Wang. Numerical method for consolidation analysis of lumpy clay fillings with meshless method. *Soils and foundations*, 44(1):125–142, 2004.

[17] LA Keith and JD Rimstidt. A numerical compaction model of overpressuring in shales. *Journal of the International Association for Mathematical Geology*, 17(2):115–135, 1985.

[18] Elena Suetnova and Guy Vasseur. 1-d modelling rock compaction in sedimentary basins using a visco-elastic rheology. *Earth and Planetary Science Letters*, 178(3-4):373–383, 2000.

[19] Christina Morency, Ritske S Huismans, Christopher Beaumont, and Philippe Fullsack. A numerical model for coupled fluid flow and matrix deformation with applications to disequilibrium compaction and delta stability. *Journal of Geophysical Research: Solid Earth*, 112(B10), 2007.

[20] Denise Bernaud, Luc Dormieux, and Samir Maghous. A constitutive and numerical model for mechanical compaction in sedimentary basins. *Computers and Geotechnics*, 33(6-7):316–329, 2006.

[21] André Brüch, Nicolas Guy, Paulo Sérgio B Lemos, and Samir Maghous. Coupled poro-mechanical tangent formulation applied to sedimentary basin modeling. *International Journal for Numerical and Analytical Methods in Geomechanics*, 46(2):221–246, 2022.

[22] Magnus Wangen. A model of fluid expulsion from compacting tight sedimentary rocks based on the toggle-switch algorithm. *Applied Computing and Geosciences*, 13:100079, 2022.

[23] JAD Connolly and Yu Yu Podladchikov. Temperature-dependent viscoelastic compaction and compartmentalization in sedimentary basins. *Tectonophysics*, 324(3):137–168, 2000.

[24] Karl Terzaghi. *A fundamental fallacy in earth pressure computations*. Number 3. Harvard University, 1936.

[25] John W Cahn and John E Hilliard. Free energy of a nonuniform system. i. interfacial free energy. *The Journal of chemical physics*, 28(2):258–267, 1958.

[26] Samuel M Allen and John W Cahn. Coherent and incoherent equilibria in iron-rich iron-aluminum alloys. *Acta Metallurgica*, 23(9):1017–1026, 1975.

[27] Ingo Steinbach. Phase-field models in materials science. *Modelling and simulation in materials science and engineering*, 17(7):073001, 2009.

[28] George J Fix. Phase field methods for free boundary problems. 1982.

[29] Robert Spatschek, Efim Brener, and Alain Karma. Phase field modeling of crack propagation. *Philosophical Magazine*, 91(1):75–95, 2011.

[30] Daniel Arndt, Wolfgang Bangerth, Bruno Blais, Marc Fehling, Rene Gassmöller, Timo Heister, Luca Heltai, Uwe Köcher, Martin Kronbichler, Matthias Maier, Peter Munch, Jean-Paul Pelteret, Sebastian Proell, Konrad Simon, Bruno Turcksin, David Wells, and Jiaqi Zhang. The `deal.II` library, version 9.3. *Journal of Numerical Mathematics*, 29(3):171–186, 2021.

[31] Kunal Bhagat and Shiva Rudraraju. Modeling of dendritic solidification and numerical analysis of the phase-field approach to model complex morphologies in alloys. *arXiv preprint arXiv:2210.14449*, 2022.

[32] Rahul Gulati and Shiva Rudraraju. Spatio-temporal modeling of saltatory conduction in neurons using poisson-nernst–planck treatment and estimation of conduction velocity. *Brain Multiphysics*, 2022.

[33] Zhenlin Wang, Shiva Rudraraju, and Krishna Garikipati. A three dimensional field formulation, and isogeometric solutions to point and line defects using toupin's theory of gradient elasticity at finite strains. *Journal of the Mechanics and Physics of Solids*, 94:336–361, 2016.

[34] Tonghu Jiang, Shiva Rudraraju, Anindya Roy, Anton Van der Ven, Krishna Garikipati, and Michael L Falk. Multiphysics simulations of lithiation-induced stress in $li_{1+x}ti_2o_4$ electrode particles. *The Journal of Physical Chemistry C*, 120(49):27871–27881, 2016.

[35] Shiva Rudraraju, Derek E Moulton, Régis Chirat, Alain Goriely, and Krishna Garikipati. A computational framework for the morpho-elastic development of molluskan shells by surface and volume growth. *PLoS computational biology*, 15(7):e1007213, 2019.

[36] K. Bhagat. Phase-field based sedimentation modeling. `https://github.com/cmmg/SedimentModeling`, 2022.

[37] Karl Terzaghi. Theoretical soil mechanics. johnwiley & sons. *New York*, pages 11–15, 1943.